An experimental study on the evolution and dispersion of a cloud of gas heavier than air

Michel Ayrault[a], Jean-Louis Balint[b] and Robert Morel[a]

[a]*Laboratoire de Mécanique des Fluides et Acoustique, B.P. 163, École Centrale de Lyon, 69131 Ecully Cedex (France)*
[b]*The University of Maryland, Department of Mechanical Engineering, College Park, MD 20742 (U.S.A.)*

(Received July 16, 1989; accepted in revised form March 23, 1990)

Abstract

This paper presents an experimental study of the evolution and dispersion of a cloud of gas heavier than air in a simulated neutral atmospheric boundary layer. First, a comparative study of instantaneous releases for two density cases of 1 and 1.87 are presented. The results were obtained by laser tomography technique. Then, we report some statistics on the fluctuating concentration field in a two-dimensional plane. The measurements were obtained by a technique based on visualization and digital image processing. The method is well suited for this type of study, provided that the number of observations is sufficient.

1. Introduction

Toxic or hazardous materials that are accidentally released near the ground create plumes or clouds of gas heavier than the surrounding air. The behaviour of such gases is very different from that of a passive gas. Because of the negative buoyancy, the cloud spreads over a large area, its internal stability reducing the vertical turbulent dispersion.

According to Hunt et al. [1], the dispersion process of a dense gas cloud released instantaneously can be divided into four distinctive phases during which different physical phenomena occur. They describe them as follows:

1. The initial phase: it is controlled by the initial conditions of the release. In this phase, two forces influence the cloud; the inertial force and the drag force exerted by the mean flow around the structure from which the release is generated. The initial Richardson number Ri_0, characterizes the ratio between these two effects.

2. The gravitational spreading phase: the motion of heavy gas is mainly horizontal. It is determined by the buoyancy and the mean atmospheric flow. During this phase, the lateral spreading of the cloud is very strong. The mixing is

only due to the internal turbulence of the cloud generated by the gravitational flow [2]. Mixing activity is mainly located on the boundary of the gravity current.

3. The nearly passive phase: as the cloud spreads out, the dispersion due to the gravity becomes less and less important compared to the dispersion caused by the external turbulence. The activity is mainly located on the top edge of the cloud.

4. The passive phase: eventually, the cloud becomes so diluted that the gravity has no more influence and the gas behaves as a passive scalar. The dispersion process is controlled only by the external turbulent flow. The phenomenon is then well described by the Gaussian theory.

Depending on the initial release conditions and on the external flow, some phases can be either combined or even avoided.

Despite the approximations it entails, the simulation of dense gas releases in a wind-tunnel enables the study of complex geometrical situations that are difficult to introduce in numerical models. Some fundamental aspects of the turbulent mechanisms can be investigated by this approach and utilized for model improvement.

The principles of dense gas simulation have been reported in the literature [3,4]. In the case of neutral atmosphere simulation, with a gas of constant physical properties, the similitude criteria involve non-dimensional parameters, such as relative density, Reynolds number and Froude number. It is not possible to respect both Froude and Reynolds numbers similitude. If the gravity effect is preponderant, it is better to respect the Froude number similitude and relative density. The turbulent Reynolds number must be made large enough to obtain an acceptable simulation of the turbulent diffusion.

The goal of this study was to simulate the instantaneous release of dense gas in neutral atmosphere. The existing techniques available for concentration measurements, such as flame ionization probe [5] and aspirating probe [6,7] are not well adapted for this kind of investigation. Moreover, they provided only point measurements. For our experiments, we utilized the technique developed by Balint et al. [8], based on flow visualization and digital image analysis. This method provides valuable information on the geometrical shape of the cloud. But, most important, it determines the spatial distribution of instantaneous concentration in a two-dimensional cross-section of the cloud and its evolution in time.

2. Experimental technique and facilities

The experiments were carried out in the EDF–ECL atmospheric diffusion wind-tunnel. On the floor of the tunnel a finite volume of gas heavier than air was released in neutral atmosphere. The gas initially consisted of an air/freon 12 mixture, of density 1.87 (relative to air). It was contained in a rectangular

box of volume $V_0 = 3130$ cm^3. The sides of the box were made of two pairs of bellows. The structure collapsed to the floor in about 0.3 second, releasing the mixture in the flow. A sketch of the release setup is shown in Fig. 1.

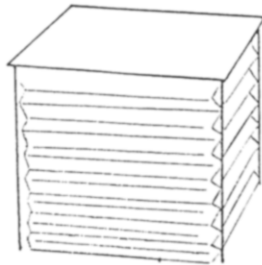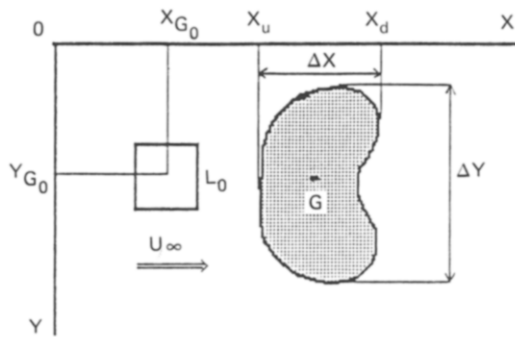It should be pointed out that the interaction of the structure containing the
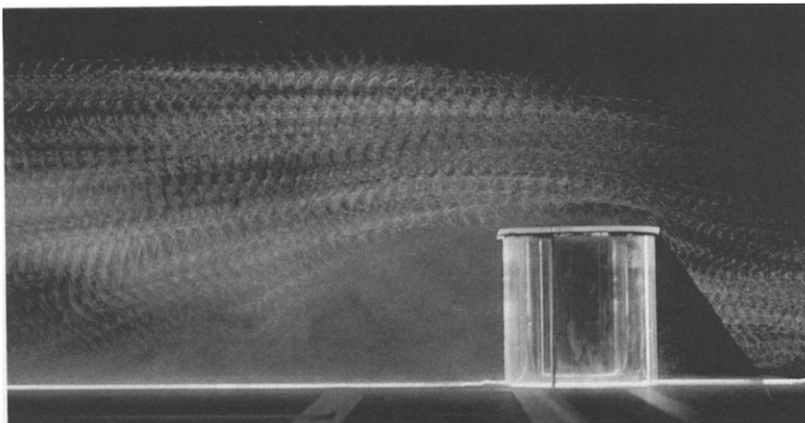

Fig. 1. Gas source structure.

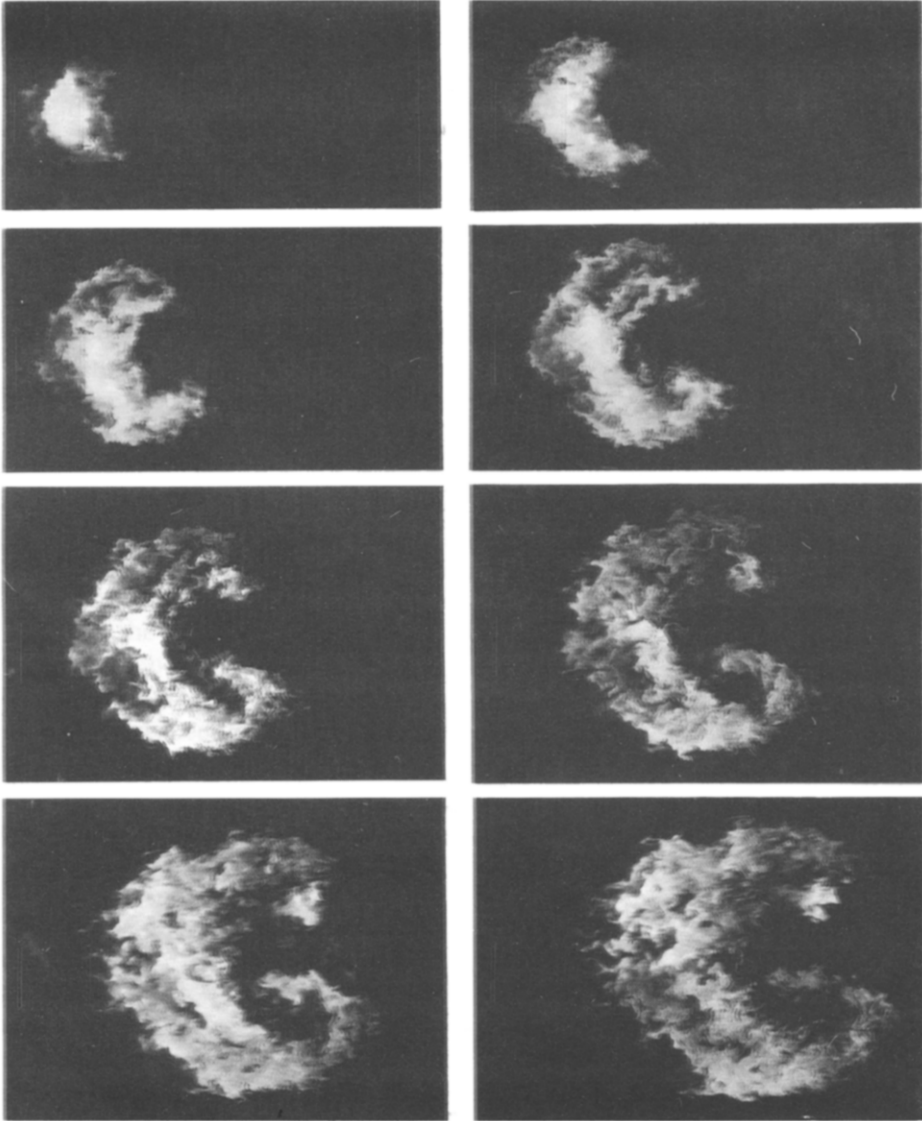Fig. 2. Wake behind the structure.

4

Fig. 3. Instantaneous images of a cloud of gas heavier than air. Horizontal cross-section. Time sequence goes from left to right and from top to bottom. Density equals 1.87, $t = 0.2, 0.4, 0.6, 0.8, 1.0, 1.2, 1.4$ and 1.6 s.

gas and the external flow plays a very important role in the initial dispersion and later evolution of the cloud. A description of such flow around a cube was given by Meroney [9]. It is also illustrated in Fig. 2 which shows the wake behind the structure and a high speed region above its top. Separation points are located at the edges of the cube, they coincide with the low pressure gen-
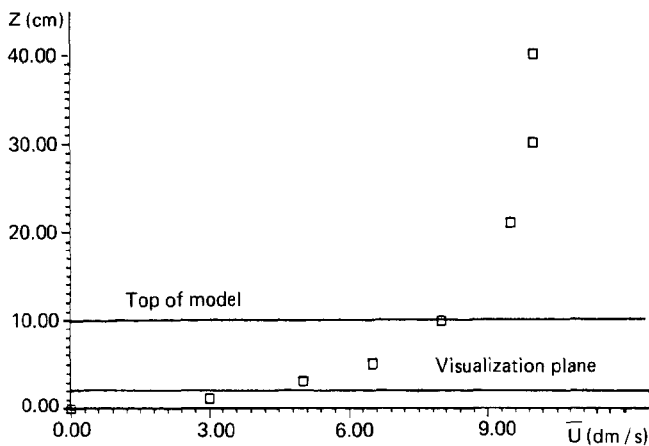
Fig. 4. Mean velocity profile.

erated by high speed regions on the side of the structure. During the release, these external characteristics produce a typical crescent-shaped cloud (see Fig. 3). The volume of dense gas collapses on the floor, spreads sideways, the upwind front travels upstream, and then, very suddenly, two counter rotating vortices appear at the downwind front. The kinematic conditions used for the flow visualization experiments were as follows:

$$U_\infty = 1 \text{ m/s} \quad u^* = 0.06 \text{ m/s} \quad z_0 = 0.25 \text{ mm}$$
$$Re_0 = 10^4 \qquad Ri_0 = 1.9$$

The laser tomography visualizations were made in a horizontal plane, two centimeters above the floor. Figure 4 shows the mean velocity profile at the initial cross-section centroid as well as the location of the light plane and the model in the boundary layer. The 5 mm thick light plane was generated by a 5 W argon laser beam which was deflected by a set of 16 rotating mirrors. As depicted in Fig. 5, the laser beam was sweeping the flow region of interest; the mirrors' rotation frequency was adjustable from 25 to 1000 Hz. Before being released into the flow, the heavy gas was seeded with fine particles of incense, the mean diameter was 0.8 μm and the standard deviation of 0.2 μm. At any given time, the particles located in the light plane scatter a certain amount of light energy. For a given volume, the amount of scattered light is proportional to the number of particles contained in that volume; this result is discussed further in Section 3.

The light sheet is recorded with a 35 mm movie camera on a high sensitivity black and white film at a rate of 25 images per second. Once developed, the film was digitized with a vidicon camera for digital image analysis purposes.
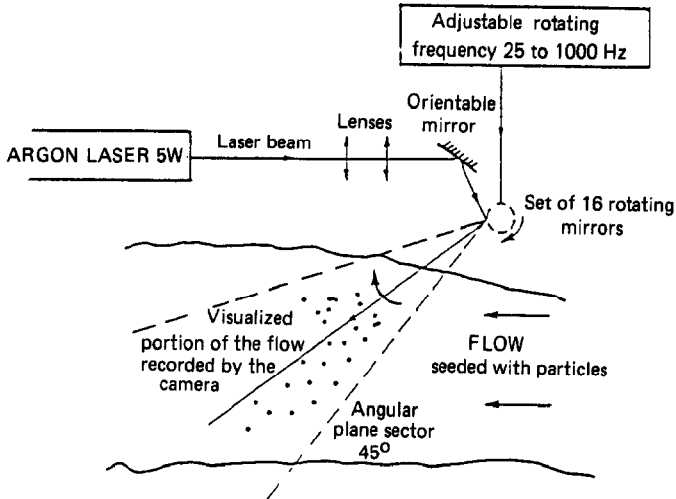
Fig. 5. Experimental setup.

For these experiments, the spatial resolution (which is a function of the observation field) was 4.5 mm. From the film optical density, usually called grey level, one can determine the particle concentration value for each point of the digitized picture by using the calibrating procedure described below. Therefore, this method provides both spatial and time evolution of the instantaneous field in a planar cross-section of the cloud.

3. Calibration method for the concentration field

In order to determine concentrations from visualization images we had to account for many non-linear phenomena related to the visualization method. These can be divided into two distinctive groups:

1. Light diffusion phenomena by the fine particles located in the light sheet such as Mie scattering [10].

2. Optical distortion and attenuation due to the various lenses and optical systems used throughout the recording process and the photographic development.

The laser beam that illuminates the incense particles can be considered as a planar monochromatic light source of wavelength λ (not completely uniform in spite of an optical system), and of luminous flux per unit area E. In the visualized portion of the flow, the elemental volume dV containing N particles scatters light energy in all directions. In the case of spherical particles, the contribution of each particle to the light intensity, dI, scattered in a given direction is characterized by I_u, the amount of light intensity scattered by a particle per unit of incident flux. I_u is a function of $\alpha = 2\pi a/\lambda$, where a is the radius of a particle. If the particles are not identical in size, a function $I_{ui}(\alpha_i)$ can be defined for each particle of radius a_i, where $\alpha_i = 2\pi a_i/\lambda$. Moreover, if the distance between the particles is sufficient, i.e., greater than at least twice their

diameter on the average, and if their distribution is random, dI can be expressed as the sum of the individual particle contributions. In this case, secondary diffusion effects can be neglected and we can write the following equation (see [10] for a detailed derivation):

$$dI = \sum_i E\pi a_i^2 N_i I_{ui}(\alpha_i) dV$$

By measuring simultaneously the scattered light, with a photomultiplier, and the number of particles, with a particle counter, we checked the above equation. The results are shown in Fig. 6.

The luminous flux p received on the 35 mm film can be expressed as a function of the scattered light energy dI contained in a solid angle dΩ_s, the medium transmissivity T_t, and the camera lens transmissivity T_0, as follows:

$$p = dI d\Omega_s T_t T_0$$

One way to account for the attenuation effects was suggested by Balint et al. [8]. It consists of sampling the uniform light plane without any injection of particles. These background pictures, once digitized and averaged, provide a background distortion map which can be used to correct the flow visualization images.

The response of a silver-based emulsion is not linear (Hurter and Driffield curve); this is the main reason that calls for film calibration. In fact, this non-linearity is amplified by another photographic phenomenon known as the reciprocity-law failure (see for instance [11]). This effect occurs for a very short
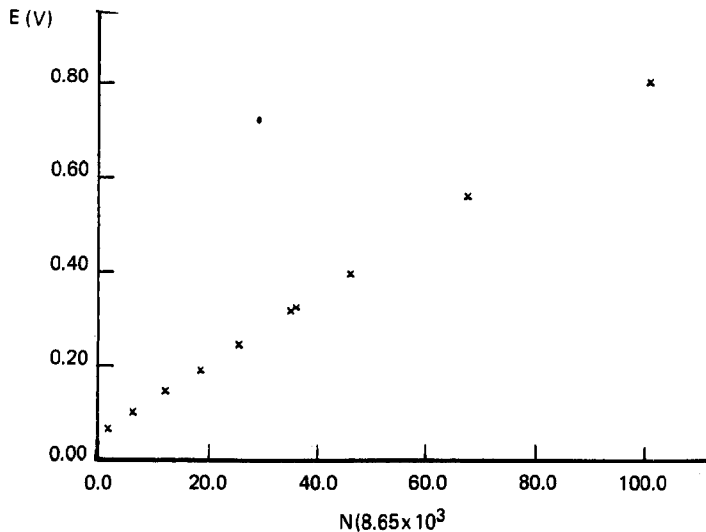

Fig. 6. Correspondence between particle counter measurements and a photomultiplier measurements.

8

time exposure of the film emulsion; this was the case for our experiments. Most of the time, we used a mirror rotation frequency of 60 Hz. At that frequency, we estimate that for an area of 1 mm^2 located at 2 m from the rotating mirrors, its exposure time during a laser beam sweep was about 1 μs. Finally, we took one last, but not least precaution which was to develop all exposed films in the same manner and in one single batch.

The relationship between grey levels and particle concentration values can be obtained either directly from reference test pictures [12,13], or indirectly, from various experimental or numerical methods. The direct method is well suitable for the study of continuous gas releases such as plumes. For instantaneous releases, we preferred the indirect method developed by Balint et al. [8]. The calibration curves shown on Fig. 7 were obtained from the numerical results of Riou [15,16] with the three-dimensional Mercure Gaz–Lourd numerical model [14]. The calibration method is described in the following steps:

1. Digitization of N instantaneous pictures, each corresponding to a given time step and described by their grey level function $Z_k(x,y)$, where k varies from 1 to N and (x,y) takes discretized values on a 512$\times$512 grid, which is the digitizer spatial resolution. With a digitizer grey level resolution of 8 bits, $Z_k(x,y)$ can assume 256 different grey values.

2. Computation of the mean grey level image, called M1, for which each pixel is defined as:
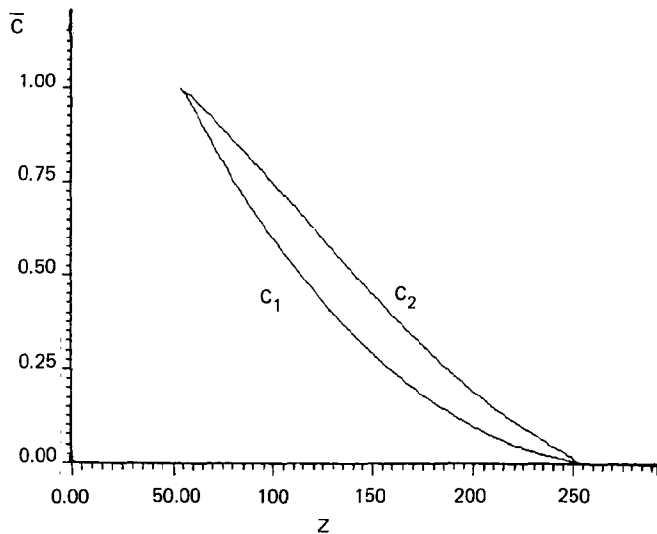

Fig. 7. Calibration curves C_1 and C_2: Correspondence between volumetric concentration and grey level values.

$$\bar{Z}(x,y) = \frac{1}{N}\sum_{k=1}^{N} Z_k(x,y)$$

3. Derivation of the calibration curve, noted C_1 (see Fig. 7): the curve establishes a correspondence between some test points of M1 grey level values $\bar{Z}(x,y)$ and the mean concentration $\langle C(x,y) \rangle$ provided by the three-dimensional model for the same locations.

4. Calibration of the N instantaneous images, using the calibration curve C_1: the value of each pixel k is changed from its original grey level Z_k, to its corresponding concentration value C_k.

5. Computation of a mean concentration image, called M2, for which each pixel is defined as:

$$\bar{C}(x,y) = \frac{1}{N}\sum_{i=1}^{N} C_i(x,y)$$

6. Calibration of the mean image M1: the mean grey levels are changed to mean concentration values. The result of this operation defines a new image called M3.

7. Comparison of M2 and M3: in order to evaluate the non-linear effects of the calibration process, we compare the mean of the calibrated images M2 to the calibration of the mean grey level image M3. If the grey level difference for each location (x,y) of M2 and M3 is less than a predefined threshold (say 5 grey levels for example), the calibration curve is validated. Otherwise, the calibration procedure is iterated one more time; which was the case for our experiments. We repeated the procedure, going back to step 3 and using image M2 in place of M1; this defined a new calibration curve C_2. We notice in Fig. 7 that this second calibration curve is almost linear. This ensured that, after two successive calibrations, we had a quite reliable representation of the instantaneous concentration field in the visualization plane.

8. Computation of higher statistical moments. Each picture is considered as one realization of the turbulent phenomenon for which standard deviation, skewness and flatness of the fluctuating concentration field can be determined. These quantities are available for each location (x,y) of the field of view.

In order to validate the technique for the study of gases heavier than air, we had to do some important and necessary checks. First, we had to verify that the incense particles markers, initially mixed with the gas, were properly following the gas flow. Numerous tests were carried out at the exit of a pipe flow. A photomultiplier measured the scattered light emitted by the solids particles; a T.S.I. aspirating probe provided the freon 12 concentration. In addition, the pipe flow was investigated by visualization and direct calibration of the films. It should be pointed out that the T.S.I. aspirating probe provides only mean concentration measurements. Figures 8 through 11 present comparisons of the
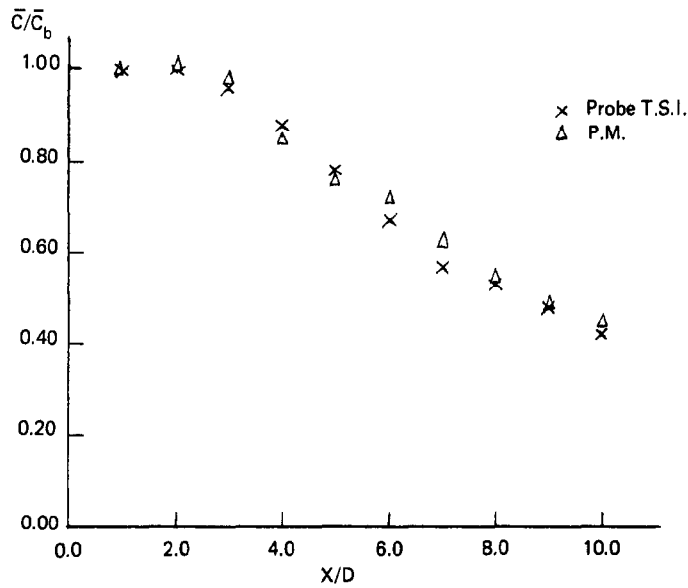
Fig. 8. Mean concentration on the axis: comparison between aspirating probe and photomultiplier. The mean concentration values at the pipe exit C are normalized with the mean concentration at the exit. The downstream x is normalized with the pipe diameter.
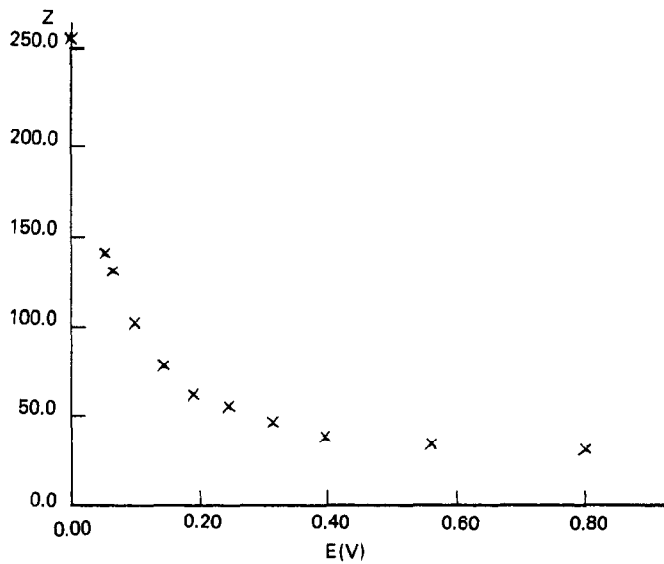

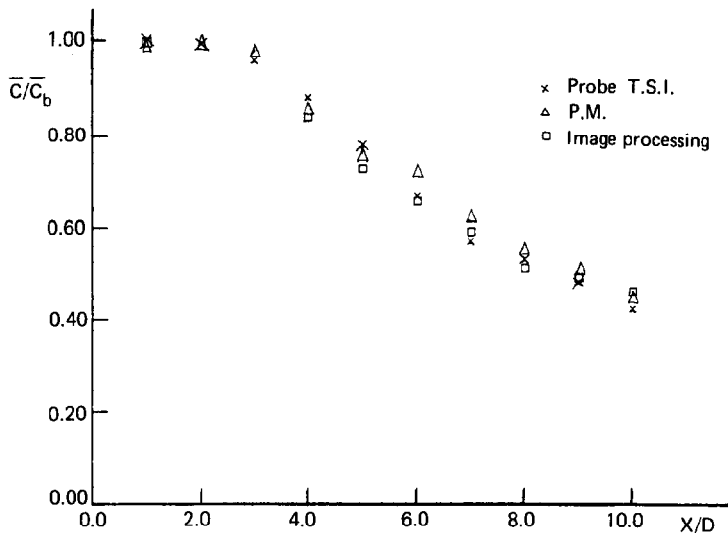Fig. 9. Direct calibration curve: correspondence between grey level values and light scattered by particles.

Fig. 10. Mean concentration on the axis: comparison between aspirating probe, photomultiplier and image processing (same normalization as in Fig. 8).
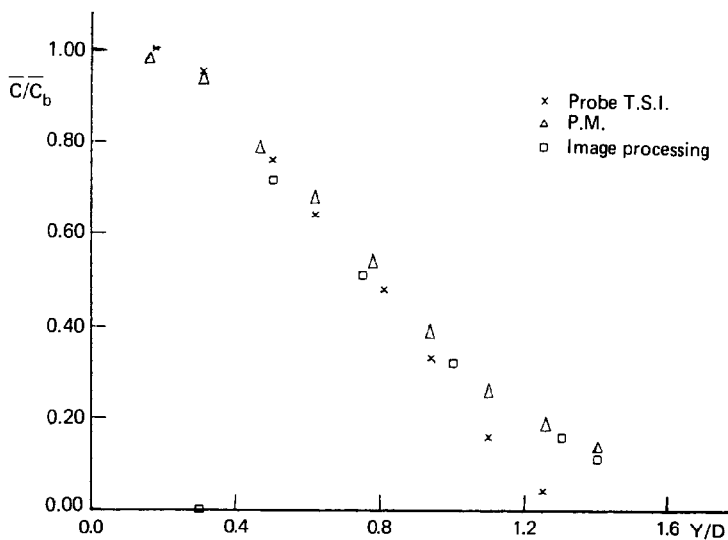

Fig. 11. Mean concentration at $x/D = 5$: comparison between aspirating probe, photomultiplier and image processing (same normalization as in Fig. 8).

results obtained with the various techniques. Figure 7 depicts the mean concentration on the axis of the release measured by aspirating probe and photomultiplier. The particle concentration is quite consistent with the freon 12 concentration. This clearly indicates that the incense particles follow the gas flow very well and that the light scattering measurements, which are propor-

tional to the number of solid particles present in a given volume, provide good measurements of the gas concentration. The direct calibration curve representing concentration versus grey level is shown on Fig. 9. The results obtained
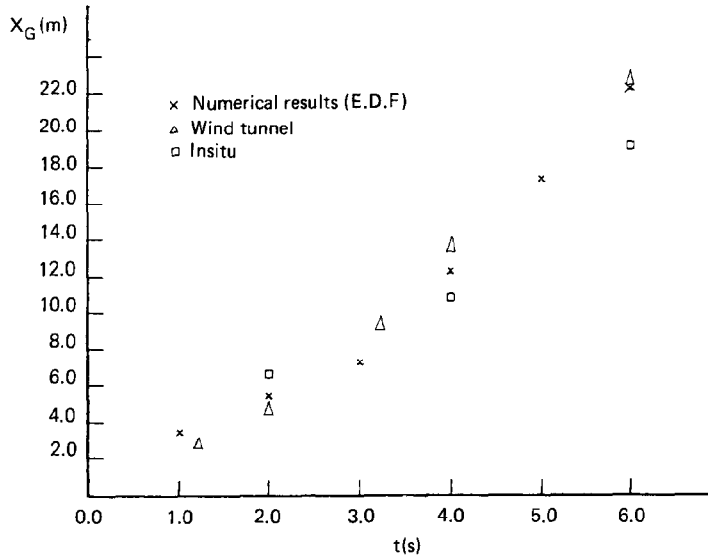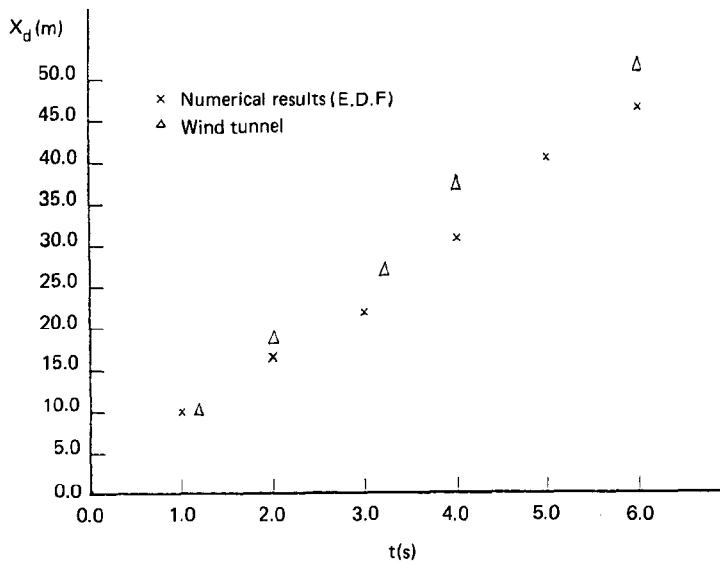

Fig. 12. Comparison of the centroid evolution.

Fig. 13. Comparison of the downwind front evolution.

by imaging technique agree very well both photomultiplier and aspirating probe techniques, they are presented in Fig. 10 and Fig. 11.

Further validation of the method was done by comparison with the *in situ* measurements of Thorney Island, trial 18 [17] and the Mercure G.L. numerical calculations of Riou [15]. We compared the evolutions of the cloud centroid and downwind front, as shown on Fig. 12 and Fig. 13, the agreement is fairly good. The small discrepancies may be due to differences in initial conditions. Differences between wind tunnel and *in situ* experiments could be on velocity profiles, shape and structure of the model, or volume of gas being released; these factors are believed to be predominant during the collapsing phase of the cloud. Also, it should be pointed out that the comparisons involve statistical mean (in the wind tunnel and numerical model cases) values determined by a single realization of the phenomenon (*in situ* experiment).

4. Experimental results

4.1 Influence of the initial gas density on the cloud dispersion: geometrical aspects

In order to have a better insight of the influence of gravity on the cloud dispersion, two series of experiments were carried out. The only parameter that differs from one series to the other was the initial density relative to air of the gas released, namely 1 and 1.87. Figure 14 shows the evolution of the mean clouds for both cases. The ensemble averages were computed on 34 identical experiments for both density cases.

We notice a significant difference in the behaviour of the cloud when its density is equal to that of the surrounding fluid. In this case, the incense particle markers act like passive scalars. The evolution of the cloud consists then of only two distinctive phases: the initial phase, entirely determined by the release initial conditions and the passive dispersion phase, which starts when the external turbulence determines the flow. According to Hunt and Rottman [1], the transition between those two phases occurs after a time T_t given by:

$$T_t = \frac{1}{9}\left(\frac{U_{10}}{u_a}\right)^2 \frac{L_0}{U_{10}}$$

where u_a is the characteristic velocity scale related to the turbulent fluctuations. If we assume $u_a/U_{10} = 0.075$, our experiment gives $T_t = 3.6$ s. This seems to indicate that all our measurements were carried out in the initial phase because they were taken between $t = 0$ s and $t = 1.6$ s. Comparisons between the averaged images of the clouds for both density cases were done on the following parameters: area, upwind and downwind front, centroid locations, width and length of the mean images.

First of all, we notice a linear evolution of the mean cloud areas, as seen on Fig. 15. The influence of gravity is quite clear as is reflected in the increase of
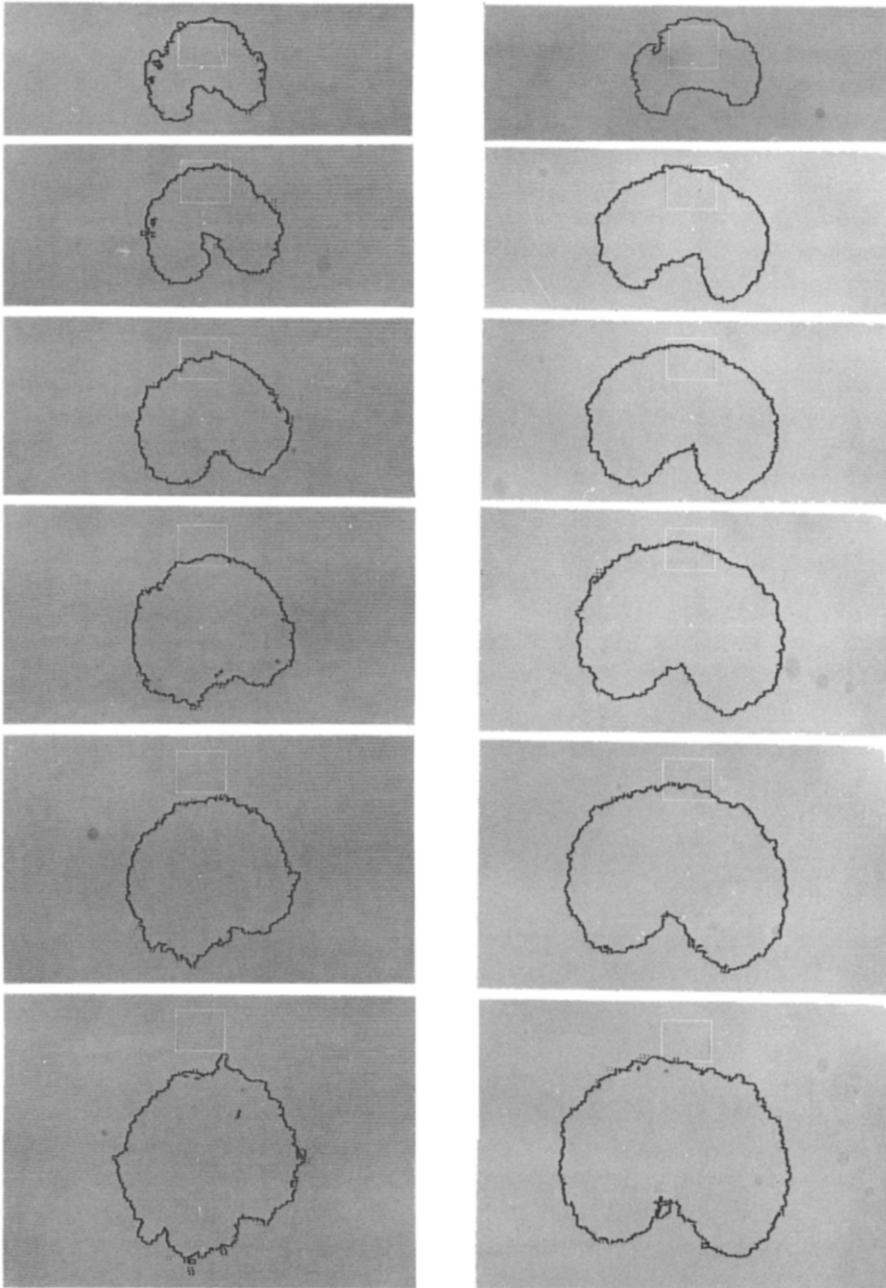
14

Fig. 14. Evolution of the ensemble mean average cloud. Time sequence goes from top to bottom. Left hand side: density is equal to 1; right hand side: density is equal to 1.87.
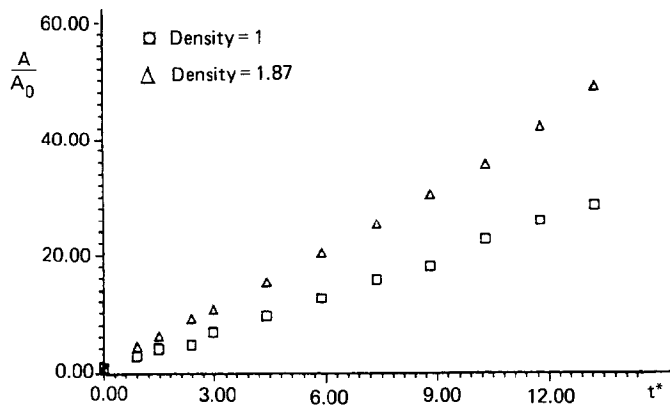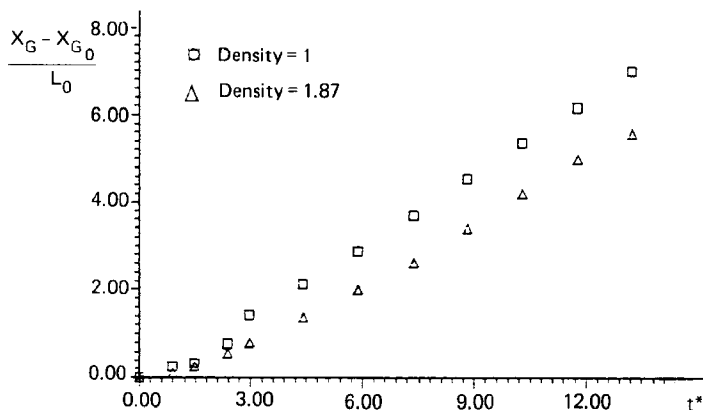
Fig. 15. Area evolution.

Fig. 16. Centroid evolution.

the area velocity, from 400 m²/s to 650 m²/s for density cases of 1 and 1.87 respectively. In contrast, for $t \leq 1$ s, the centroids evolve in the same manner, as shown in Fig. 16, the gravity being significant only later on. As far as the upwind front evolution of the cloud is concerned, we notice in Fig. 17 that it first moves upstream, stabilizes, and then goes in the direction of the flow, reaching the mean velocity of the flow in the visualization plane (i.e. 4 m/s). In the passive scalar case (density of one), this motion can only be due to the initial conditions induced by the model opening method. When the pairs of bellows collapses onto the floor, counterrotating vortices are generated on the sides of the box. These vortices have enough energy to move upstream. For the density case of 1.87, buoyancy amplifies this motion even more. The ideal conditions of instantaneous release are not fully simulated, this causes the initial phase to interact with the gravity spreading phase. It is interesting to notice on Fig. 18 that the downwind front evolves quite identically for both density
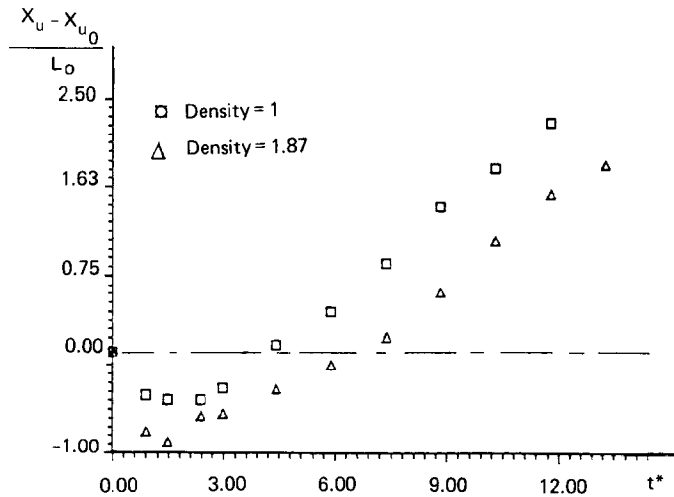
$$\frac{X_u - X_{u_0}}{L_0}$$

Fig. 17. Upwind front evolution.
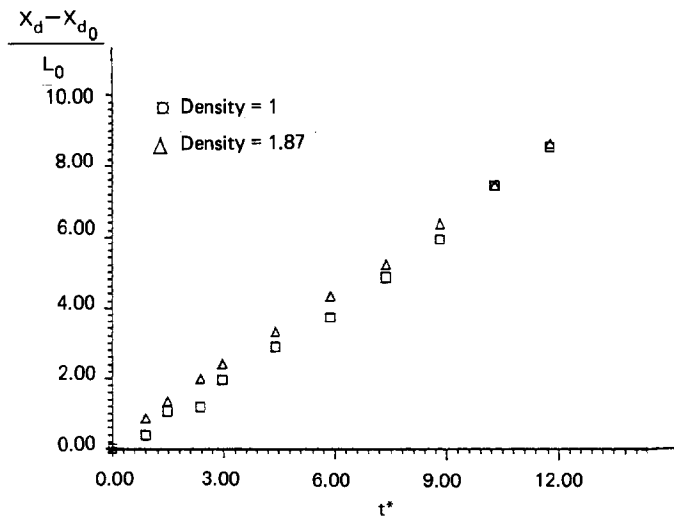
$$\frac{X_d - X_{d_0}}{L_0}$$

Fig. 18. Downwind front evolution.

cases; it moves much faster than the local mean velocity. This is probably due to the wake of the cloud which generates fluid momentum transfer between the top and lateral sides of the cloud. This seems to be confirmed by the width evolution of the clouds presented in Fig. 19a. The discontinuity observed in the time evolution of the downwind front, for the passive scalar case, can be explained by the pairing of counterrotating vortices, as clearly can be seen in Fig. 14. This causes an artificial increase of the downwind front location and
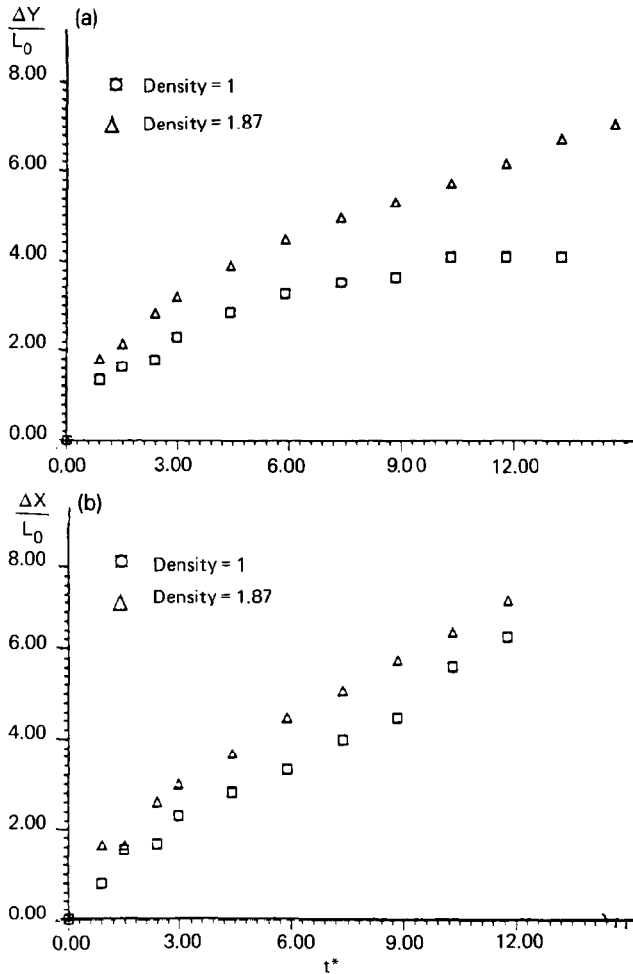
Fig. 19a. Width evolution.
Fig. 19b. Length evolution.

length as can be seen in Fig. 19b. The effects of the releasing mechanism on the cloud evolution probably cease at about the same time.

4.2 Evolution of the concentration

This instantaneous release of a finite volume of gas heavier than air in an atmospheric boundary layer wind tunnel is a random phenomenon. Although the overall behavior of the cloud is always the same (collapse onto the floor due to buoyancy, lateral spreading, conversion of potential energy into kinetic energy and upstream motion of the upwind front), the local variation of concentration in space and time varies drastically from one release to the other,
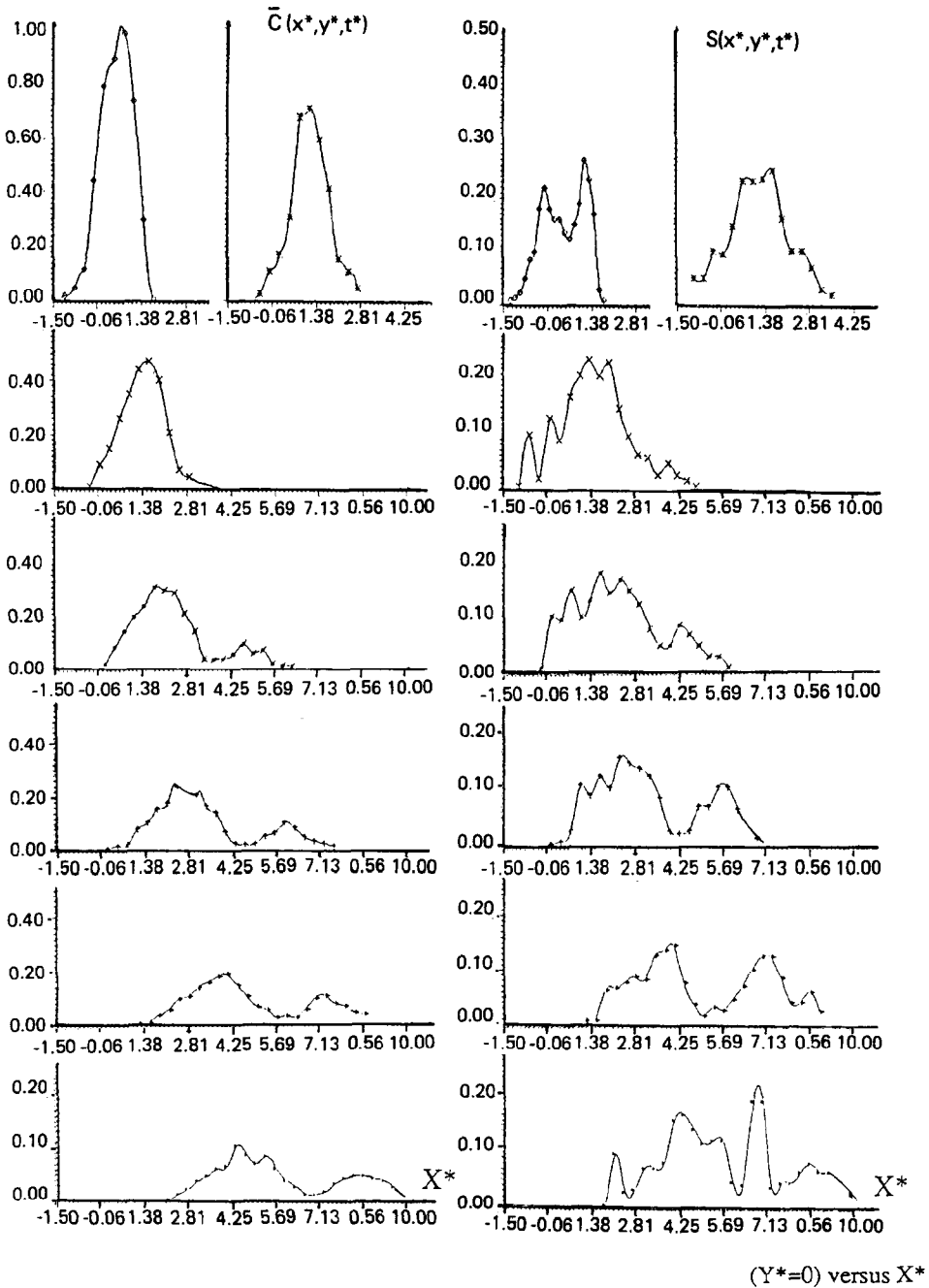
18

Fig. 20. Mean and root-mean-square (R.M.S.) concentrations profiles on the release's axis
($Y^*=0$) versus X^* at different times t^*. ($t^*=2.94$, 5.88, 7.35, 8.8, 10.3, 13.2, 14.7.)
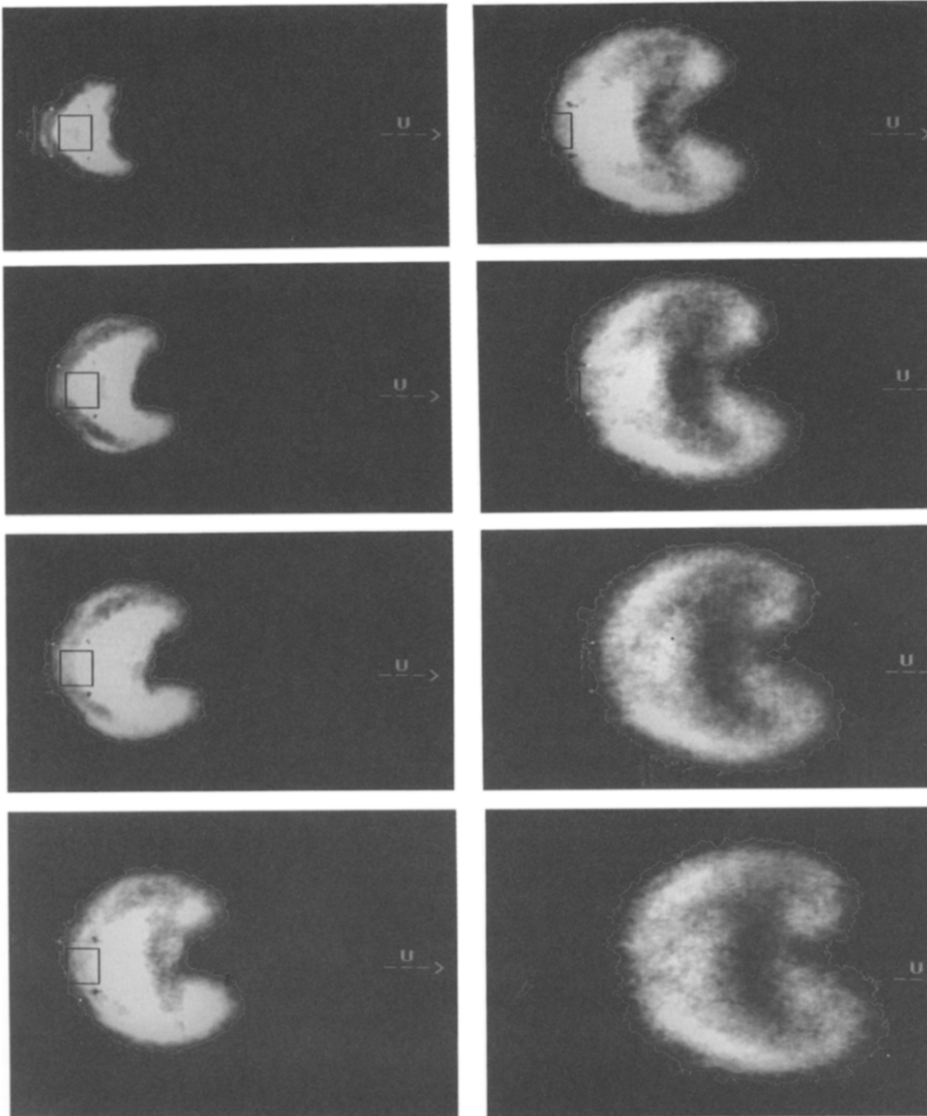
(a)

Fig. 21a. Mean concentration images; $t^* = 1.47$, 2.94, 4.4, 5.88, 7.35, 8.8, 10.3, 11.76.

even under identical initial conditions. Chatwin [20] clearly showed that knowledge of the average concentration field is not sufficient to describe the dispersion completely. If we model the instantaneous concentration $C(x,y,t)$ by a random variable, we need to provide information on its higher order moments, as well as its probability density.
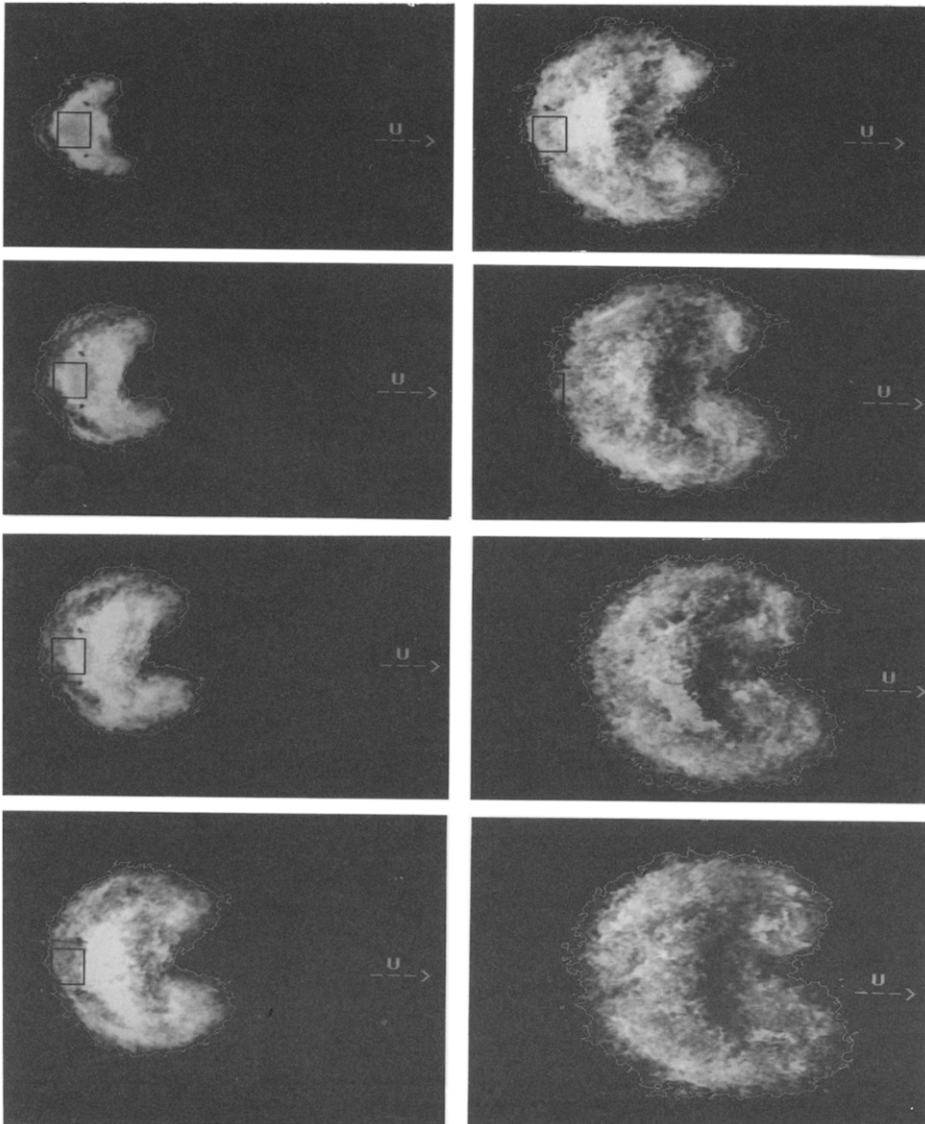
(b)

Fig. 21b. Standard deviation concentration images; $t^* = 1.47, 2.94, 4.4, 5.88, 7.35, 8.8, 10.3, 11.76$.

Meroney and Lohmeyer [6] carried out a wind tunnel study of freon 12 with density 4.2. They used an aspirating probe and recorded the concentration maxima during the passage of clouds of different volume. Although their statistical analysis was done on a small number of experiments, it revealed a strong
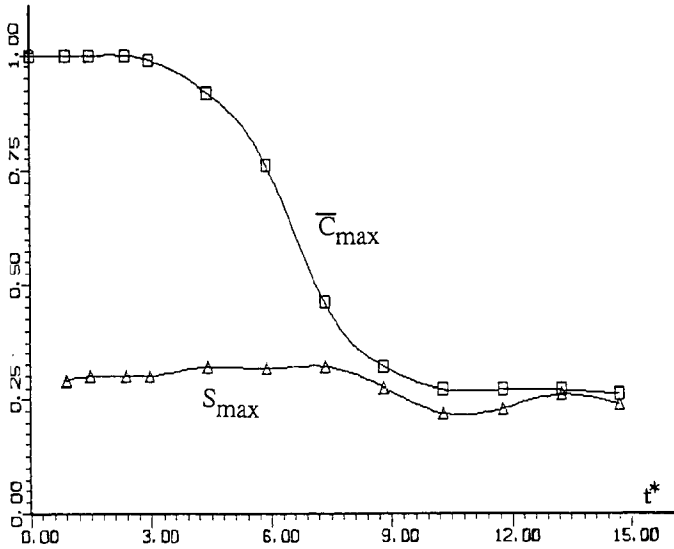
Fig. 22. Maximum values of C and S inside the mean clouds versus time t^*.

dispersion and a tendency for the mean vertical concentration profiles to be Gaussian. Our visualization method enables us to examine the turbulent dispersion characteristics in much more details. We generated a series of 34 identical releases of initial density 1.87 and initial Richardson number of 1.9. Therefore, for each time step following the release, a total population of $N=34$ samples was available for statistical analysis. The pictures were calibrated according to the method previously described (Fig. 20).

An unbiased estimate of the mean and standard deviation can be written as follows:

$$\bar{C}(x,y,t) = \frac{1}{N}\sum_{i=1}^{N} C_i(x,y,t)$$

$$S(x,y,t) = \left[\frac{1}{N-1}\sum_{i=1}^{N} \{C_i(x,y,t) - \bar{C}(x,y,t)\}^2\right]^{1/2}$$

If we assume $C(x,y,t)$ to be a Gaussian distribution, then classical statistical analysis [18] provides an expression for the confidence intervals which contain $\bar{C}$ and S within $(1-2\alpha)$ %. They are given by:

$$\left(\bar{C} - \frac{t_\alpha S}{\sqrt{N}}, \bar{C} + \frac{t_\alpha S}{\sqrt{N}}\right) \quad \text{and} \quad \left(\frac{(N-1)S^2}{\chi_\alpha^2}, \frac{(N-1)S^2}{\chi_{\alpha-1}^2}\right)$$

where t_α and χ_α^2 are the Student and the χ^2 distribution at $(N-1)$ degrees of freedom. Carn and Chatwin [19] showed that, even if the distribution is not
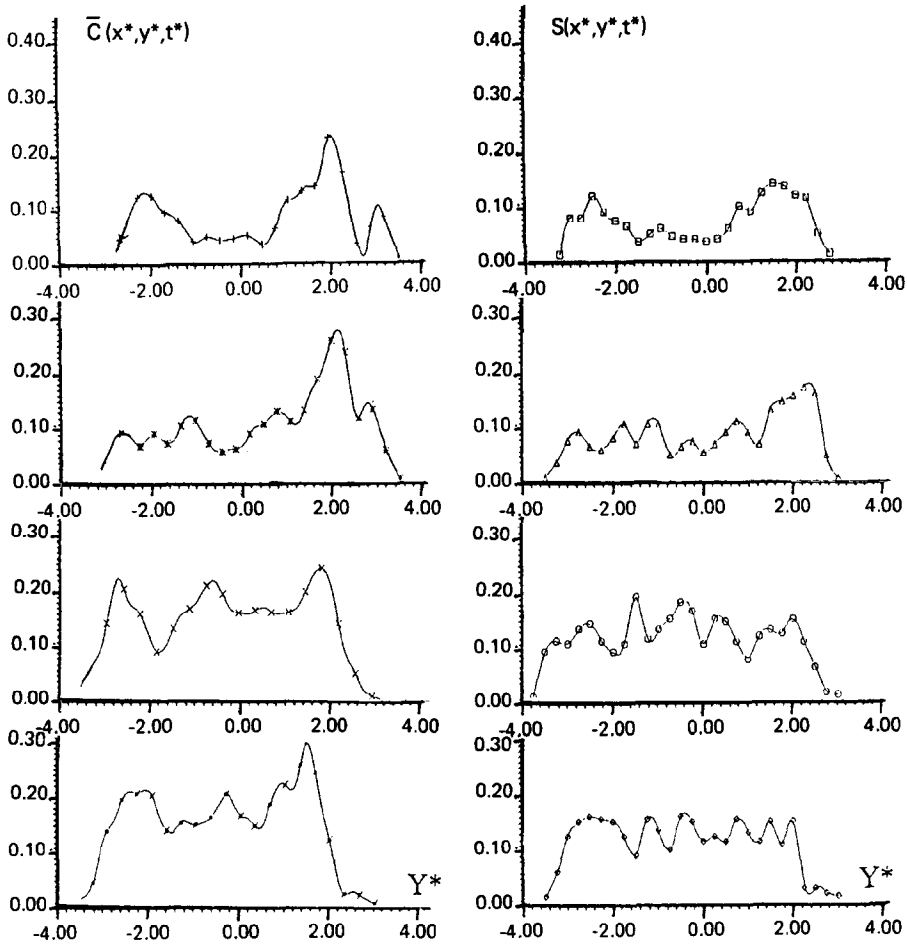
Fig. 23. Mean and root-mean-square (R.M.S.) concentration profiles at $x^* = 3$ versus y^* at different times t^* ($t^* = 7.35$, 8.8, 10.3, 11.8).

Gaussian, the central limit theorem ensures that the estimates can be valid with a good degree of accuracy. In the case where $2\alpha = 0.05$ and $N = 34$, the half width of the confidence interval on the mean concentration is equal to 0.035. In contrast, the 80% confidence interval ($2\alpha = 0.2$) on the standard deviation has a precision of about 30% only. Clearly, it is much easier to achieve a good precision on the estimate of the mean than for the standard deviation. Moreover, as the order increases, the accuracy on the higher order statistical moments becomes even worse. Therefore, given the rather small number of samples available, we restricted our study to the mean and standard deviation only (first and second moment, Figs. 21a and b).

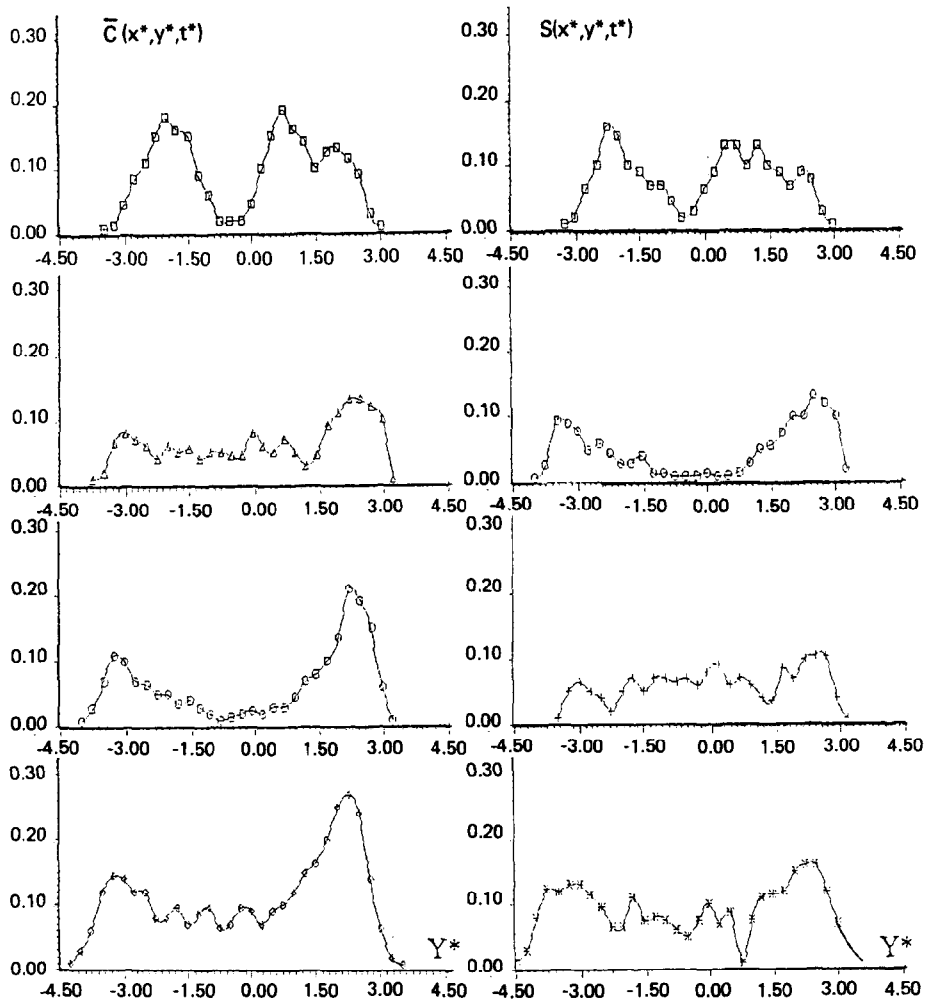Figure 20 shows the evolution of the measured mean concentration $\bar{C}(x^*,0,t^*)$

Fig. 24. Mean and R.M.S. concentration profiles at $x^*=5$ versus y^* at different times t^* ($t^*=8.8$, 10.3, 11.76, 13.28).

and of the standard deviation $S(x^*,0,t)$ along the release axis ($y^*=0$) for different time steps. We notice that, up to $t^*\leqslant 7$ ($t<1$ s), the shape of the mean is quite similar. This reflects the fact that the cloud is still influenced by gravity and initial conditions alone. Fig. 22 presents the maxima of $\bar{C}$ and S for different time steps. They indicate that the cloud spreads rapidly, with a weak dispersion on its boundaries and a strong global dilution; the standard deviation $S(x,y,t)$ displays fairly large values throughout the release. Another interesting feature of the maximum values of S is that they remain roughly the same for the different time steps, as seen in Fig. 22. Consequently, the variability,
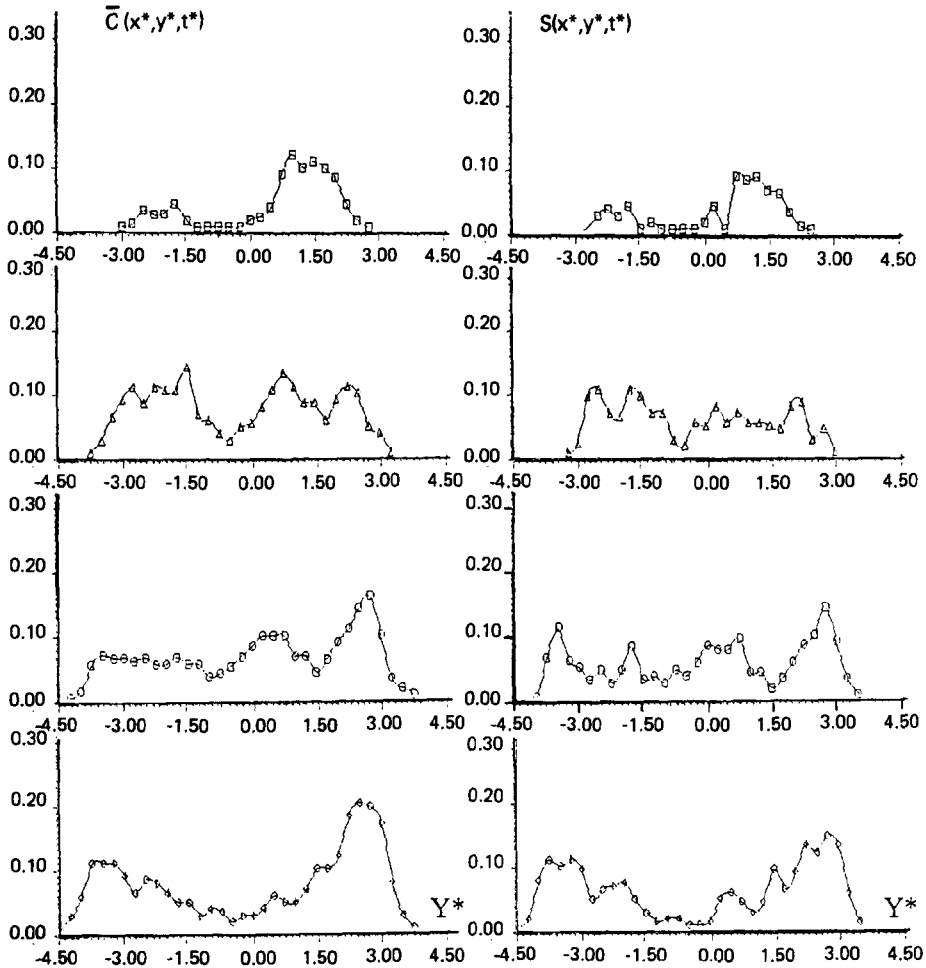
24

Fig. 25. Mean and R.M.S. concentration profiles at $x^* = 7$ versus y^* at different times t^* ($t^* = 10.3, 11.76, 13.23, 14.7$).

defined by the ratio $I = S/\bar{C}$, is quite large and always greater or equal to unity. This is consistent with the visual aspect of the cloud. Near the floor, it looks like an unbroken patch. As we go higher, the patch is randomly broken up. Holes appear, regions become stretched and pinched off. All these mechanisms are responsible for an increase in the variability.

Figures 23, 24 and 25 depict the profiles of $\bar{C}$ and S at different time steps and for different locations, $x^* = 3, 5, 7$. It is quite obvious that the cloud is still in the gravitational spreading phase. The dispersion on the boundary is weak, even for $x^* = 7$ and $t^* = 14.7$. In future experiments, we are planning to inves-

tigate the nearly passive phase as well. In a first step, we will be using more simple initial conditions.

5. Conclusions

The visualization technique associated with the digital image processing has proved to be a powerful tool for the mean and turbulent concentration fields study. It provides a detailed insight of the turbulent dispersion process. The statistical moments, up to the second order are presented for the entire visualization plane; accurate measure of the higher order moments requires a larger number of samples. With this method, the effects of the initial gas density on the dispersion of clouds were also studied. In particular, we described quantitatively their geometrical characteristics. From these results, we determined that the gravitational spreading phase occurs at a very short non-dimensional time value of about 8. For future experiments, we are planning to study the phenomenon beyond the gravity spreading phase and document the nearly passive phase.

6. Acknowledgements

References

1   J.C.R. Hunt, J.W. Rottman and R.E. Britter, Some physical processes involved in the dispersion of dense gases, in: G. Ooms and H. Tenekes (Eds.), Atmospheric Dispersion of Heavy Gases and Small Particles, I.U.T.A.M. Symposium, Proceedings, Delft, 1983, Springer-Verlag, Berlin, 1984, pp. 361-391.

2   R.E. Britter and J.E. Simpson, Experiments on the dynamics of a gravity current head, J. Fluid Mech., 88 (1978) 223-240.

3   R.N. Meroney, Guidelines for fluid modeling of dense gas cloud dispersion, J. Hazardous Materials, 17 (1987) 23-46.

4   D.J. Hall, Wind-tunnel modelling of heavy gas spills, Warren Springs Laboratory, Dept. of Industry, Stevenage, Hertfordshire (1982).

5   R.E. Britter and W.H. Snyder, Fluid modelling of dense gas dispersion over a ramp, J. Hazardous Materials, 18 (1988) 37-67.

6   R.N. Meroney and A. Lohmeyer, Statistical characteristics of instantaneous dense gas clouds released in an atmospheric boundary layer wind-tunnel, Bound. Layer Meth., 28 (1984) 1-22.

7   G. Konig, M. Schatzmann and A. Lohmeyer, Measurements of gas concentration fluctuations in wind tunnel simulations, in Proc. 7th Int. Conf. on Wind Eng., Aachen, 1987.

8   J.L. Balint, M. Ayrault and J.P. Schon, Quantitative investigation of the velocity and concentration fields of turbulent flows combining visualization and image processing, in: J. Wang (Ed.) , Flow Visualization III, pp. 254-258.

9   R.N. Meroney, Turbulent diffusion near buildings, in: E. Plate (Ed.), Engineering Meteorology, Elsevier, Amsterdam, 1982.

10   J. Kerker, The Scattering of Light and Other Electromagnetic Radiation, Academic Press, New York, NY, 1979.

11   T.H. James, The Theory of The Photographic Process, Macmillan, New York, NY, 1959.

12   E. Alcaraz and M. Ayrault, Wind-tunnel simulations of instantaneous release of heavier-than-air gases, I.C.E.A., Lausanne, 1987.

13   D.J. Schlien, Instantaneous concentration field measurement technique from flow visualization photographs, Exp. Fluids, 6 (1988) 541-546.

14   Y. Riou and A. Saab, A three dimensional numerical model for the dispersion of heavy gases over complex terrain, Report E.D.F. HE 32-85-12, 1985.

15   Y. Riou, Comparison between MERCURE-GL code calculations, wind-tunnel measurements and Thorney-Island trials, J. Hazardous Materials, 16 (1987) 247-265.

16   Y. Riou, The use of a three dimensional model for simulating Thorney-Island field trials, in J.S. Puttock (Ed.) Stably Stratified Flow and Dense Gas Disperions, Clarendon Press, Oxford, 1988.

17   J. McQuaid, Objectives and design of the phase I heavy gas dispersion trials, in: J. McQuaid (Ed.), Heavy Gas Dispersion Trials at Thorney Island, J. Hazardous Materials, 11 (1985) 1-33.

18   A.E. Mace, Sample-size Determination, Reinhold, New York, NY, 1964.

19   K.K. Carn and P.C. Chatwin, Variability and heavy gas dispersion, J. Hazardous Materials 11 (1985) 281-300.

20   P.C. Chatwin, The use of statistics in describing and predicting the effects of dispersing gas clouds, J. Hazardous Materials 6 (1982) 213-230.

Notation

U_∞	external velocity
U_{10}	mean velocity at 10 cm from the floor
V_0	volume of the model
u^*	friction velocity
Z_0	roughness length
G	centroid
$L_0 = (V_0)^{1/3}$	length scale
$T = \{V_0)^{1/3}/g_0'\}^{1/2}$	time scale
$t^* = t/T$	adimensional time
$x^* = (x - x_{G_0})/L_0$	adimensional X-coordinate
$y^* = (y - y_{G_0})/L_0$	adimensional Y-coordinate
$Re_0 = U_\infty L_0/v$	initial Reynolds number
$Ri_0 = g_0' L_0/U_{10}^2$	initial Richardson number
g_0'	initial modified gravity
$C(x,y,t)$	instantaneous volumetric concentration
$\bar{C}(x,y,t)$	mean concentration
$S(x,y,t)$	standard deviation concentration